

GREEN SYNTHESIS OF Fe₃O₄ STRUCTURES USING *Euterpe oleracea* MART EXTRACT FROM THE LEGAL AMAZON, BRAZIL**Simara F. Borges^a, Karollyne S. Andrade^a, Evilly C. Vaz^a, Manoel D. Morais Neto^a, Aluisio A. Cabral^b, Eledir V. Sobrinho^c, Cláudia Q. da Rocha^d and Gilvan P. de Figueredo^{a*,*}**^aDepartamento de Química, Instituto Federal de Educação, Ciência e Tecnologia do Maranhão, 65030-005 São Luís – MA, Brasil^bDepartamento de Física, Instituto Federal de Educação, Ciência e Tecnologia do Maranhão, 65030-005 São Luís – MA, Brasil^cInstituto de Química, Universidade Federal do Rio Grande do Norte, 59078-970 Natal – RN, Brasil^dDepartamento de Química, Universidade Federal do Maranhão, 65080-805 São Luís – MA, Brasil

Received: 10/28/2023; accepted: 01/25/2024; published online: 03/20/2024

The synthesis of oxides using plant extracts as precursors has attracted attention as it is an economical, efficient, and ecological route. *Euterpe oleracea* Mart, available in the Legal Amazon, has great potential due to its composition, rich secondary metabolites. Therefore, this work aimed to investigate the potential of aqueous açá leaf extract as precursors in synthesizing Fe₃O₄-type oxides. The synthesis was developed in two stages to obtain the hematite phases (step 1) and the magnetite phase (step 2). The effect of pH on phase formation and structure was evaluated in step 1. Then, the material was obtained in step 2 by precipitation with pH adjustment. The powders were characterized by thermal analysis, X-ray diffraction, infrared spectroscopy, and scanning electron microscopy. The results showed that pH played a significant role in the thermal behavior, crystallite sizes, and structural parameters of hematite, with neutral or acidic pH being more attractive for obtaining crystallites between 21 and 24 nm. Magnetite with 21.51 nm crystallites was precipitated, indicating possible capping of the Fe₃O₄ particles and preserving their magnetic characteristics.

Keywords: green chemistry; açá; nanostructures; α -Fe₂O₃; Fe₃O₄.**INTRODUCTION**

The Brazilian Amazon comprises the largest extension of continuous humid forests on the planet, around 3,700 km², and covers more than 5 million km² of the national territory. It is characterized by its extensive river networks, dense vegetation cover, and incomparable biological richness. It is recognized as the most prominent Brazilian biome and one of the most crucial biodiversity reserves in the world. Moreover, the Legal Amazon has an area of 5,217,423 km², representing 61% of the Brazilian territory. In addition to containing the entire Brazilian Amazon biome, it contains 20% of the Cerrado biome and part of the Mato Grosso Pantanal. It encompasses the whole states of Acre, Amapá, Amazonas, Mato Grosso, Pará, Rondônia, Roraima and Tocantins and part of the state of Maranhão.^{1,2}

The oxides have been previously synthesized through various methods, including sol-gel, hydrothermal, co-precipitation, microwave, and combustion. However, with the increasing population growth rate and industrial factories, recent efforts have been focused on utilizing more eco-friendly synthesis methods to prevent environmental pollution and minimize harmful chemical residues.³ Thus, there has been an increasing interest in the search for ecologically friendly synthesis methods in the literature.⁴⁻⁶ Green chemistry and its 12 principles seek to ensure a process with a low level of waste generation following conscientious and sustainable behavior.⁷ The biggest obstacle in developing synthetic methods that adhere to these principles is the complete or partial replacement of ecologically hazardous solvents with those that provide little to no risk.⁸

Within this context, green chemistry is a interdisciplinary scientific field that concentrates on the design, development, and execution of chemical processes. Green chemistry aims to enhance the sustainability of chemical products, reducing their impact on human health and creating a greener future.⁹⁻¹¹

Green synthesis uses alternative, less harmful environmental inputs using low-cost, less toxic, and less dangerous products. It consists of using enzymes, amino acids, algae, microorganisms, and plant extracts as organic precursors for synthesizing nanostructures from different categories of materials. In this sense, some compounds extracted from plants can function as chelating, polymerizing, stabilizing, and capping agents for the synthesis mechanisms of metal oxide nanostructures.¹²

There are several biological sources used in this type of synthesis. However, the use of plant extracts is the most reported in the literature since the biomolecules or phytochemicals products present in these extracts can interact with the metal cations of the precursor salt through chelation and polymerization mechanisms, similar to what happens in the reaction medium of classical methodologies used for the synthesis of metal oxides, such as sol-gel and polymeric precursors or modified Pechini.^{3,13}

The green synthesis of nanostructures produced from plant extracts is carried out in an easy and fast reaction, marked by a change in the medium's color. Synthesis can be observed in three phases: activation, growth, and termination. Nanostructures combine in the growth phase, forming a range of morphologies that can influence their properties.¹⁴

Iron oxide nanostructures are interesting since they can be found in various environments ranging from aquatic and terrestrial systems to different natural ecosystems. They consist of combinations of the chemical elements iron (Fe) and oxygen (O) and come in various forms, such as magnetite (Fe₃O₄), maghemite (γ -Fe₂O₃), and hematite (α -Fe₂O₃). These iron-based structures have distinct physicochemical properties, are highly available in nature, and have low toxicity. It has been possible to verify an extensive study of iron oxides in recent years for applicability with adjustable anticorrosive, optical, and magnetic properties, in addition to presenting excellent chemical stability and biocompatibility, high surface/volume ratio, large specific surface area, and easy separation.¹⁵ Thus, iron oxides are

*e-mail: gilvanfigueredo@ifma.edu.br

highly valued in several industrial applications, covering both the food and pharmaceutical industries, due to these unique characteristics. Their versatility and special properties make them promising materials for various uses.¹⁶

The plant species *Euterpe oleracea* Mart (Arecaceae) is native to the Amazon's lowland regions and abundant in Maranhão, Brazil. It belongs to the palmaceae group, considered one of the most productive in this ecosystem. Açaí is exploited from it, a fruit much required for food purposes due to its organoleptic and nutritional characteristics and the presence of compounds with antioxidant and anti-inflammatory properties.¹⁷ The use of dry straw from *Euterpe oleracea* leaves is limited, and there are no studies on its use to add value to this abundant biomass. However, recent studies show that several phenolic compounds of hydroxycinnamic acid are found in the leaf extract, as well as apigenin di-C-glycosides (ACGs), a group of flavonoids,¹⁸ secondary metabolites such as phenols, tannins, steroids, triterpenes, resins, catechins, saponins and alkaloids, anthocyanins and anthocyanidins.¹⁹ Therefore, studies where these biomolecules become necessary and competitive for different applications are required, mainly using the green synthesis of metal oxides assisted by biomolecules from plant extracts.

Therefore, we investigated the potential of the aqueous extract of açaí leaves (*Euterpe oleracea* Mart) to be used as a natural organic precursor in synthesizing Fe_xO_y -type structures in this paper. The α - Fe_2O_3 and Fe_3O_4 oxides synthesized in this work are of interest in the chemical and pharmaceutical industries, among others.

EXPERIMENTAL

Plant material

The leaves of *Euterpe oleracea* plants were collected in São Luís, Maranhão (2°35'57.0"S 44°12'09.1"W), Legal Amazon region, Brazil. The collection followed Brazilian biodiversity protection and registration laws in the National System of Genetic Heritage and Associated Traditional Knowledge (SisGen No. A04BFAE).

Obtaining and chemical characterization of the extract

The leaves were washed with distilled water, dried in the open air for 72 h, and ground in a knife mill. Then, 3 g of leaf powder was mixed with 300 mL of distilled water and left under constant stirring for 4 h at 60 °C. After filtration, the aqueous leaf extract was collected and used in green synthesis.

The extract previously frozen at -10 °C was freeze-dried for chemical investigation to remove all the aqueous solvents. For high-performance liquid chromatography (HPLC) analysis, the extract went first through the clean-up stage via solid phase extraction (SPE) to eliminate interfering substances. A Strata C-18 silica cartridge (500 mg 6 mL⁻¹, Phenomenex, Torrance, USA) activated with 3 mL of methanol (MeOH, Sigma-Aldrich, Munich, Germany) was used. In this case, 0.0060 g of the extract was dissolved in 1.0 mL of MeOH. Next, the dissolved sample was transferred to the SPE cartridge (6 mL), eluted with 1.0 mL of MeOH, and subjected to a cold jet drying process until complete evaporation of the solvent. Then, they were solubilized in 1.0 mL MeOH and filtered through a polypropylene microfilter (Millipak®, Darmstadt, Germany) with a 0.45 µm pore size. The clean extract was analyzed on a Shimadzu chromatograph (model LC-20AT - Prominence) with a diode array detector (DAD), also from the same brand (model SPD-M20A). A Kinetex C18 column (250 mm × 4.6 mm, 5 µm, 100 Å), Phenomenex brand (Torrance, USA) was used. The mobile phase consisted of water acidified with 0.01% formic acid (Sigma-Aldrich, Munich, Germany) (A) and

methanol acidified with 0.01% formic acid (B). The exploratory gradient was used as an elution mode, in which the concentration of B varied in the range of 5 to 100% in 95 min, at a flow of 0.9 mL min⁻¹, temperature of 28 °C, and with an initial pressure of 160 kgf cm⁻². The volume of the injected sample was 20 µL.

Liquid chromatography-electrospray ionization tandem mass spectrometry (LC-ESI-IT-MS) was performed using a spectrometer (Bruker, Massachusetts, USA). Chromatographic analysis was performed on a Luna 5 µm C18 100 Å column (250 × 4.6 mm, Phenomenex, Torrance, USA). The binary gradient mobile phase consisted of 0.1% formic acid (Sigma-Aldrich, St. Louis, USA) in water (solvent A) and 0.1% formic acid in methanol (Sigma-Aldrich, St. Louis, USA) (solvent B). Compounds were eluted from the analytical column with a 50 min gradient ranging from 5 to 100% solvent B at a constant flow rate of 1 mL min⁻¹ in 30 min.

Data acquisition was performed in positive and negative ionization mode, with fragmentation in several stages (MS2 and MS3), according to the following parameters: nebulization gas pressure 50.0 psi; capillary temperature 300 °C; transfer capillary input voltage -4500 V; desolvation gas N₂, flow of 10 L min⁻¹; collision gas He, acquisition range, *m/z* 50-1200. Raw data were analyzed using Data Analysis 4.3 software (Bruker, Massachusetts, USA).

Synthesis of the Fe_xO_y structures

The Fe_xO_y structures were synthesized to obtain the hematite phases (step 1) and the magnetite phase (step 2). The synthesis started in step 1 by adding $Fe(NO_3)_3 \cdot 9H_2O$ to the *Euterpe oleracea* extract. The extract reaction with nitrate was performed under constant stirring at 90 °C until a gel formation occurred. Samples were synthesized at pH 5, 7, and 10 to evaluate the effect of pH on phase formation and particle morphology. To adjust the pH, 0.1 mol L⁻¹ HCl (Synth, Diadema, SP) was used for pH 5, and 1 mol L⁻¹ NH₄OH (Synth, Diadema, SP) for pH 7 and 10. The gels were pre-calcined at 250 °C for 120 min at a rate of 10 °C min⁻¹ to obtain the organic-inorganic precursors (EAçaí- Fe_2O_3). Then, they were calcined at 500 °C for 120 min at a rate of 10 °C min⁻¹ to form the structure. Otherwise, aqueous solutions of $FeCl_2 \cdot 4H_2O$ and $FeCl_3 \cdot 6H_2O$, 0.1 mol L⁻¹ were employed in step 2. The synthesis consisted of mixing the aqueous extract and chloride solutions in a 3:4 ratio (extract/solutions). The extract was slowly dripped into the chloride mixture, and the reaction was conducted under constant stirring for 60 min at 50 °C. The pH of the mixture was adjusted with 1 mol L⁻¹ NH₄OH (Synth, Diadema, SP) until the precipitate formed. The suspension was left to rest for 2 h, centrifuged at 3.000 rpm for 20 min, and vacuum-filtered. The obtained solid was dried at 60 °C for 24 h (ppt- Fe_3O_4).

Characterization of the oxides

Thermogravimetric (TG/DTG) and differential scanning calorimetry (DSC) analyses were simultaneously performed on a Netzsch STA-449C analyzer, starting from room temperature up to 900 °C at a heating rate of 10 °C min⁻¹ using a platinum crucible and synthetic air atmosphere. Characterization by X-ray diffraction was performed using a Shimadzu XRD-6100 diffractometer, CuK α radiation source ($\lambda = 1.5406$ Å) 30 KV and 30 mA, angular scanning of 20-80° (2 θ), scanning speed of 2° min⁻¹ and step of 0.02°. The mean crystallite size was calculated using the Scherrer equation (Equation 1) and Rietveld refinement with the GSAS program. Fourier transform infrared spectroscopy measurements were performed on a Shimadzu IRAffinity-1 analyzer, equipped with a HATR MIRacle module and ZnSe prism, with a scan of 400-4000 cm⁻¹, resolution of 4 cm⁻¹ and ATR mode. The particle morphology was observed by

scanning electron microscopy using a Hitachi tabletop microscope TM-3000 microscope.

$$T_c = \frac{k\lambda}{\beta \cos\theta} \quad (1)$$

where T_c is the size of the crystallite (nm), k the Scherrer constant (0.89), λ the wavelength of the radiation used in the equipment (in nm), β the width at half height (FWHM) of the diffraction peak, and θ is the Bragg diffraction angle in degrees.

RESULTS AND DISCUSSION

Chemical characterization of the aqueous extract

Figure 1 shows the chromatogram obtained by HPLC of the aqueous extract of *Euterpe oleracea* leaves. Table 1 presents the compounds identified in the chromatogram and elucidated by mass spectrometry.

The compounds found agree with the results of Laurindo *et al.*¹⁸ and Sprenger *et al.*¹⁹ The former authors demonstrated that in the aqueous extract of the leaves, several phenolic compounds of hydroxycinnamic acid are found, including 3-*O*-caffeoylquinic acid,

4-*O*-caffeoylquinic acid and 5-*O*-caffeoylquinic acid, in addition, the açai leaf contains apigenin di-*C*-glycosides (ACGs), a group of flavonoids including 6,8-di-*C*-hexosyl apigenin; 6,8-di-*C*-hexosyl apigenin sulfate; 6-*C*-hexosyl-8-*C*-pentosyl apigenin isomers; 6-*C*-glucosyl luteolin or homoorientin; 6-*C*-pentosyl-8-*C*-hexosyl apigenin isomers; 8-*C*-glucosyl luteolin; and 6-*C*-glycosyl apigenin. On the other hand, Sprenger *et al.*¹⁹ concluded that açai fruit extracts present secondary metabolites such as phenols, tannins, steroids, triterpenes, resins, catechins, saponins and alkaloids, anthocyanins, and anthocyanidins.

Figure 2 shows an example of a route that the molecules identified in the extract usually go through during fragmentation.

The mechanism of the reaction and the formation of metal oxide structures in plant extract solutions have not yet been entirely determined. Previous results have shown that compounds in the plant extract solutions, such as proteins, phenols, and flavonoids, can bind to the metal as chelating agents, yielding the formation of the metal-phenolate complex. The stability of metal oxide structures can be described based on the interaction between the surface of the metals with the amino group and free carboxylic acid. Additionally, the proteins present in the environment prevent the accumulation and contribute to the stability of Fe_xO_y by covering the nanostructures during the green synthesis reaction. A complexing agent functions

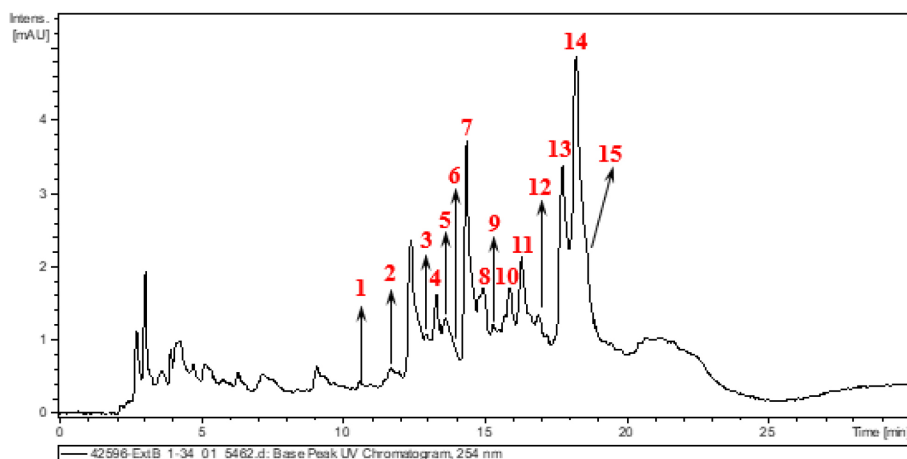


Figure 1. UV-Vis chromatogram at 254 nm of *Euterpe oleracea* leaf extract

Table 1. Compounds identified in *Euterpe oleracea* leaf extract

Peak	Retention time / min	Compound	References
1	10.7	apigenin isomer 6- <i>C</i> -(4''-acetyl)-pentosyl-8- <i>C</i> -pentoside	Cao <i>et al.</i> ²⁰
2	11.7	apigenin isomer 6- <i>C</i> -(4''-acetyl)-pentosyl-8- <i>C</i> -pentoside	Cao <i>et al.</i> ²⁰
3	12.9	apigenin 6- <i>C</i> -(2''- <i>O</i> -pentosyl)-hexosyl-8- <i>C</i> -hexoside	Zhong <i>et al.</i> ²¹
5	13.6	apigenin 6,8- <i>C</i> -dihexoside	Cao <i>et al.</i> ²⁰
6	13.9	luteolin 6- <i>C</i> -hexosyl-8- <i>C</i> -pentoside	Cao <i>et al.</i> ²⁰
7	14.4	apigenin 6- <i>C</i> -(4''-acetyl)-pentosyl-8- <i>C</i> -pentoside	Cao <i>et al.</i> ²⁰
8	15	apigenin 6- <i>C</i> -hexosyl-8- <i>C</i> -pentoside	Cao <i>et al.</i> ²⁰
9	15.3	apigenin isomer 6- <i>C</i> -(4''-acetyl)-pentosyl-8- <i>C</i> -pentoside	Cao <i>et al.</i> ²⁰
10	15.8	luteolin 7- <i>O</i> -sulfate-6,8- <i>C</i> -dihexoside	Brunschwig <i>et al.</i> ; ²² Nematallah <i>et al.</i> ²³
11	16.4	apigenin isomer 6- <i>C</i> -(4''-acetyl)-pentosyl-8- <i>C</i> -pentoside	-
12	16.9	apigenin 7- <i>O</i> -pentosyl-8- <i>C</i> -hexoside	Zhong <i>et al.</i> ²¹
13	17.7	apigenin 7- <i>O</i> -sulfate-6,8- <i>C</i> -dihexoside	Brunschwig <i>et al.</i> ²²
14	18.2	apigenin 7- <i>O</i> -sulfate-6,8- <i>C</i> -dihexoside isomer	Brunschwig <i>et al.</i> ²²
15	18.5	apigenin 7- <i>O</i> -sulfate-6,8- <i>C</i> -dihexoside isomer	Brunschwig <i>et al.</i> ²²

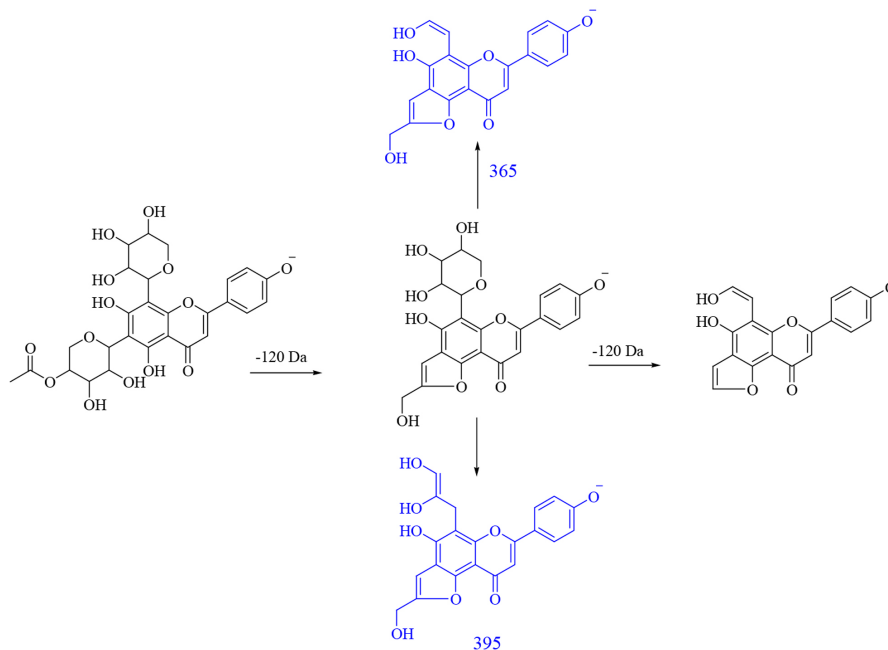


Figure 2. Fragmentation route of apigenin 6-C-(4'-acetyl)-pentosyl-8-C-pentoside. In blue, the ions of MS^3 are expressed, and in black, the ions of MS^2

similarly to a modified sol-gel process, which chelates metal cations in the solution and uniformly mixes them on an atomic scale.^{3,24}

Thermal analysis

Figures 3 and 4 present the mass loss measurements and the thermal events related to the precursors (EAçaí- Fe_2O_3 pH 5, 7, and 10) and the precipitate (ppt- Fe_3O_4), respectively. Figure 3 shows that the mass loss percentage tends to increase with the increasing pH of the precursor synthesis reaction (EAçaí- Fe_2O_3 pH 5, 7, and 10). The highest residual mass yield of 96.18% was observed for the synthesis carried out at pH 5, clearly being a consequence of the lower content of free or weakly adsorbed water on the surface of the sample, characterized by the lower percentage of mass loss in event I, as shown in Figure 4 and Table 2. Therefore, when prepared in an alkaline medium with pH adjusted with ammonium hydroxide, the precursors present a more significant layer of water.

Figure 4 presents the TG/DTG/DSC curves of the EAçaí- Fe_2O_3 precursors obtained at pH 5 (Figure 4a), pH 7 (Figure 4b), and pH 10 (Figure 4c), and of the ppt- Fe_3O_4 precipitate (Figure 4d), where it is possible to observe four well-defined mass loss events for each

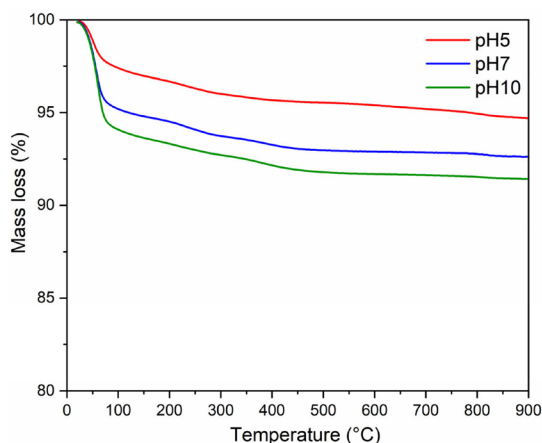


Figure 3. Thermogravimetric curves of the (EAçaí- Fe_2O_3) precursors obtained at pH 5, 7, and 10

sample. As can be seen in Table 2, at event I, all the samples presented the highest mass loss percentage. This endothermic event observed for all DTG/DSC curves in Figure 4 may be associated with the loss of free or weakly adsorbed water on the surface of the samples. It is possible to observe that events II, III, and IV for the precursor material (EAçaí- Fe_2O_3) are exothermic, discrete, and with slow mass loss. Events II and III are associated with: (i) decomposition of organic extract molecules (Table 1) remaining in the precursor; (ii) decomposition of nitrate residues that were not eliminated during pre-calcination; (iii) transformation from the amorphous to the crystalline phase of γ - Fe_2O_3 . Event IV corresponds to the γ - Fe_2O_3 to α - Fe_2O_3 (hematite) phase transformation.²⁵ Notably, the sample synthesized at pH 10 showed a higher mass loss percentage in event I (5.57%) and lower in event IV (0.09%), indicating the high thermal stability of the final phase at temperatures higher than 500 °C. According to the literature,²⁶ the pH of the green synthesis reaction plays a crucial role in the morphology of metal oxide particles due to the different activation modes of the biomolecules present in the extract and their interactions with metal cations in solution. These interactions may explain the differences observed in the thermal behavior of the samples synthesized in this work.

In addition, it is possible to observe a mass loss equivalent to 12.76% for the precipitate (ppt- Fe_3O_4), with more evident exothermic events II, III, and IV and more significant mass loss than those observed for the hematite precursors (EAçaí- Fe_2O_3). This result indicates that the magnetite precipitate particles (ppt- Fe_3O_4) may be capped or encapsulated by the molecules of the extract (Table 2). However, it presents a yield of approximately 87% in terms of magnetite (Fe_3O_4), similar to that observed in recent work published in the literature that used an extract from *Rhus coriaria*.²⁷

X-ray diffraction

Figure 5 presents the X-ray diffractograms of the samples synthesized in step 1 to obtain the hematite-type Fe_2O_3 structure. It is possible to observe narrow and well-defined diffraction lines for all samples, with a principal plane (104) at $2\theta \sim 33^\circ$, characteristic of the rhombohedral α - Fe_2O_3 phase, according to crystallographic file (Joint Committee on Powder Diffraction Standards) JCPDS

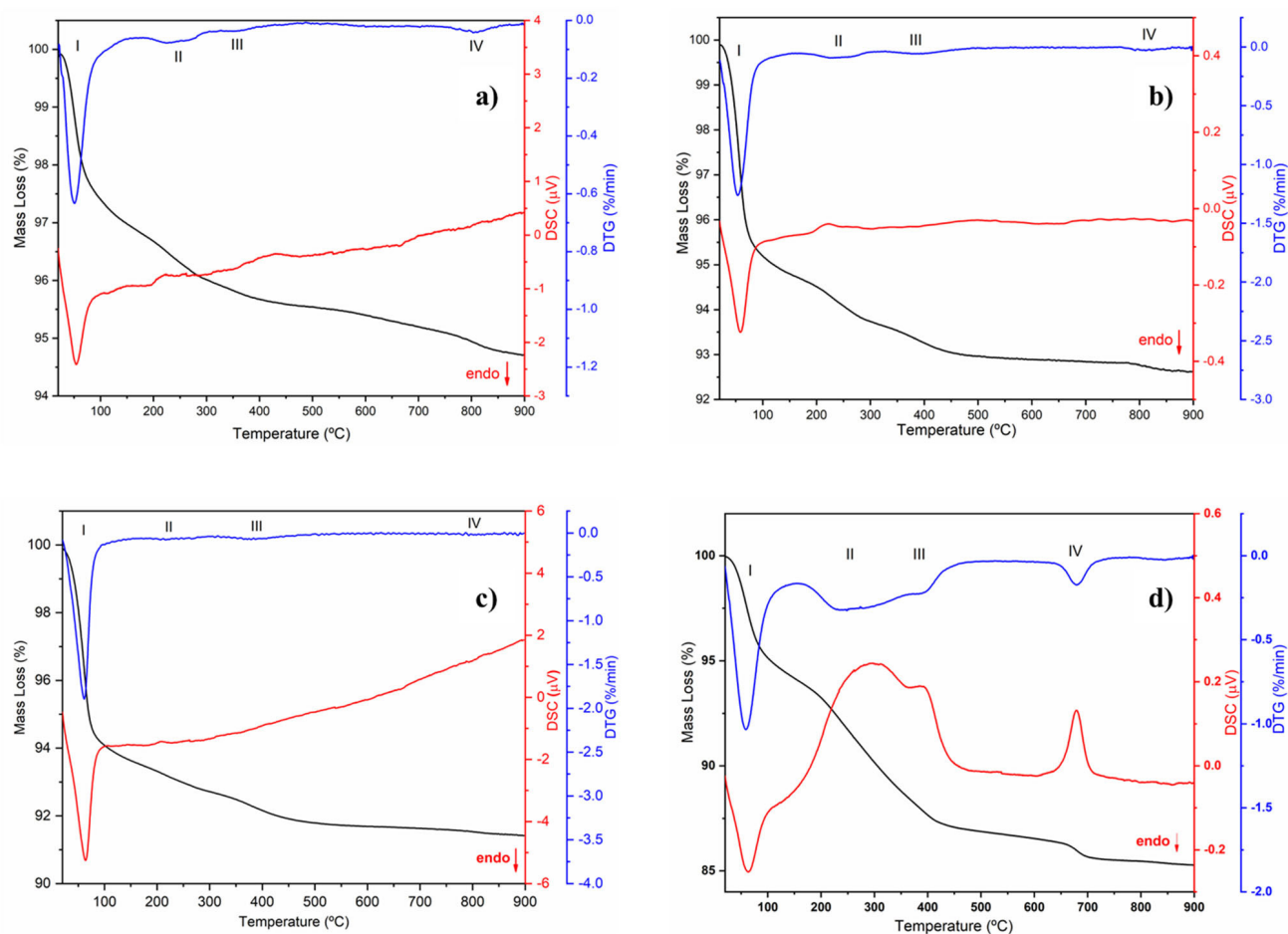


Figure 4. TG/DTG/DSC curves for the EAçaí-Fe₂O₃ precursors obtained at (a) pH 5, (b) pH 7, (c) pH 10, and for the (d) ppt-Fe₃O₄ precipitate

Table 2. List of thermal events, temperature intervals, and their respective mass losses for the EAçaí-Fe₂O₃ precursors obtained at pH 5, 7, and 10, and for the ppt-Fe₃O₄ precipitate

Event	Temperature range / °C				Mass loss / %			
	Fe ₂ O ₃			Fe ₃ O ₄	Fe ₂ O ₃			Fe ₃ O ₄
	pH 5	pH 7	pH 10		pH 5	pH 7	pH 10	
I	22-93	21-91	22-97	21-114	2.41	4.62	5.75	5.21
II	189-301	173-298	192-278	117-346	0.73	0.92	0.56	4.8
III	316-390	322-474	324-450	356-426	0.24	0.29	0.69	1.39
IV	752-860	768-867	781-849	651-713	0.33	0.19	0.09	1.32
	Residual mass / %				96.18	93.86	92.78	87.24

No. 01-079-1741. The mean crystallite sizes (CS) of the α -Fe₂O₃ phase obtained at pH 5 (23.76 nm) and pH 7 (21.39 nm) were smaller than those commonly observed in the literature.²⁷⁻²⁹ The crystallite size at pH 10 achieved 42.74 nm. This behavior indicates a strong effect of the pH of green synthesis on the crystallization mechanism of the hematite, making it more attractive to use pH 7 or 5, depending on the desired yield in terms of hematite mass (Table 2).

Figure 6 presents the X-ray diffractogram of the sample synthesized in step 2 to provide the magnetite-type Fe_xO_y structure. It can be observed that the diffraction lines correspond to the crystallographic planes of magnetite (Fe₃O₄) with cubic structure and Fd-3m symmetry, according to crystallographic file JCPDS No. 00-088-0866, with evidence for the crystallographic plane (311) at $2\theta \sim 35.5^\circ$. The identified phase has an average crystallite size of 21.51 nm, indicating the high potential of synthesis via precipitation with *Euterpe oleracea* extract in obtaining small Fe₃O₄ particles when

compared to those obtained with *Rhamnidium elaeocarpum* extract,³⁰ potato extract³¹ and *Moringa oleifera* extract.³² The synthesis is simple and relatively low cost, mainly due to energy savings, as there is no need for heat treatment of the material.

A quick test with a magnet was performed, and as can be seen in Figure 6, the particles were attracted by the applied magnetic field.

The Rietveld refinement results obtained from XRD data (Figures 5 and 6) are presented in Table 3. The refinement was convergent, with acceptable parameters for metallic oxides, indicating that a single crystalline material formed with 100% volumetric fraction and nanometric crystallites. According to the data in Table 3, it is possible to notice that all values referring to the lattice parameters and unit cell volume of the hematite samples are higher than those observed for the standard sample in JCPDS No. 01-079-1741, indicating increasing atomic distances during the crystallization process. On the other hand, an opposite behavior was observed for the magnetite sample

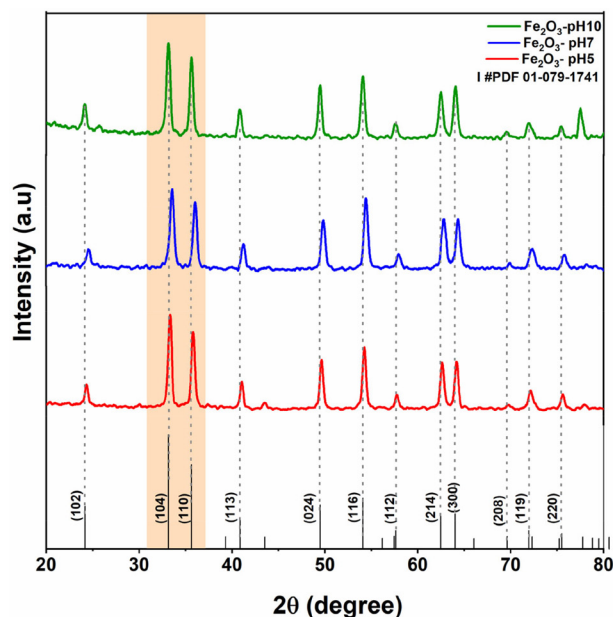


Figure 5. X-ray diffraction patterns of samples provided at pH 5, 7, and 10 and calcined at 500 °C for 120 min

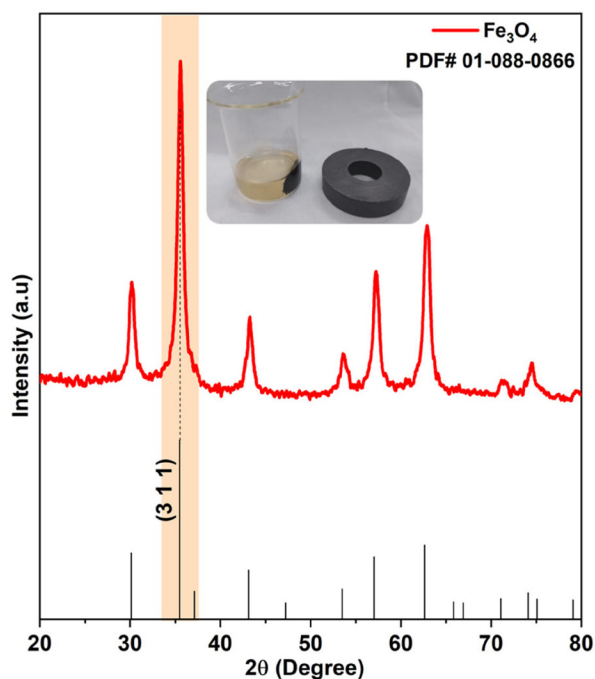


Figure 6. X-ray diffraction pattern of the sample obtained via precipitation in step 2

with more excellent atomic approximation, which the decrease of the lattice parameters and unit cell volume can justify. The considerations made based on the Rietveld refinement results developed in this work have a significant role in elucidating the microstructural behavior of iron-based oxides that are synthesized by alternative green synthesis strategies with plant extracts based on the sol-gel principle and coprecipitation, as applied in step 1 and 2, respectively.

Fourier-transform infrared spectroscopy (FTIR)

The vibrational analysis in the infrared region presented in Figure 7 for the α - Fe_2O_3 samples highlights the calcination effects. Samples of pre-calcined precursors present bands between 3900-3200 and 1700-1200 cm^{-1} , attributed to the O-H stretching of alcohols, phenols, and adsorbed water, C=O stretching (carboxylic acids), and vibration of the C-O group (alcohols and esters).³³ The absence of these bands in the calcined samples is noticeable, as well as the appearance of bands between 800-400 cm^{-1} , which can be attributed to metal-oxygen bond³⁴ vibrations of the hematite structure, mainly for the synthesized samples at pH 5 and 7.

Figure 8 presents the FTIR spectrum of the Fe_3O_4 sample, where the presence of bands between 3700-2500 and 1775-1300 cm^{-1} correspond to the O-H stretching of alcohols, phenols, and adsorbed water, stretching C=O (carboxylic acids), and vibration of the C-O group (alcohols and esters).³³ Bands between 800-400 cm^{-1} can also be seen, indicating the formation of Fe-O bonds and confirming the achievement of the magnetite structure. These results corroborate the thermal analysis data, indicating possible compounds from *Euterpe oleracea* extract capping or encapsulating the magnetite particles. Metal oxide capping has been identified as an essential strategy for stabilizing nanostructures and maintaining their performance in a given application.¹⁴

Scanning electron microscopy (SEM)

Micrographs of the samples are shown in Figures 9a-9h. All hematite samples (Figures 9a-9f) present morphology as blocks containing irregular surfaces, voids, and agglomerates. It was impossible to observe the effect of pH on the morphology of the synthesized particles. Otherwise, micrographs of magnetite reveal massive blocks with regular surfaces (Figures 9g-9h).

CONCLUSIONS

Nanocrystalline hematite (α - Fe_2O_3) and magnetite (Fe_3O_4) structures were obtained through green synthesis using aqueous *Euterpe oleracea* Mart leaf extract containing phenolic compounds and secondary metabolites. Rietveld's refinement confirmed the formation of single crystalline phases, in which unit cells were higher

Table 3. Microstructural data obtained by Rietveld refinement for the synthesized samples

Sample	Lattice parameters				Crystal system	Density / (g cm^{-3})	Refinement parameters			Volume of cell / \AA^3
	a = b / \AA	c / \AA	$\alpha = \beta$ / ($^\circ$)	γ / ($^\circ$)			wRp	Rp	χ^2	
01-079-1741	5.0342	13.7460	90	120	rhombohedral	5.27				301.69
Fe_2O_3 -pH 5	5.0394	13.7656	90	120	rhombohedral	5.25	0.38	0.29	1.66	302.75
Fe_2O_3 -pH 7	5.0464	13.7806	90	120	rhombohedral	5.09	0.38	0.31	1.18	303.93
Fe_2O_3 -pH 10	5.0355	13.7540	90	120	rhombohedral	5.32	0.33	0.24	1.18	301.99
01-088-0866	8.3847		90		cubic	5.22				589.47
Fe_3O_4	8.3366		90		cubic	5.30	0.23	1.09	1.19	579.38

wRp: weighted profile R-factor; Rp: expected R-factor; χ^2 : fitting quality factor.

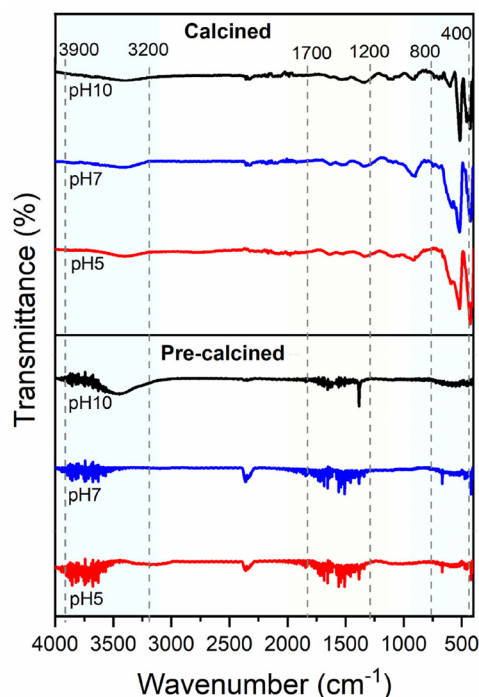


Figure 7. Infrared spectra of hematite samples obtained at pH 5, 7 and 10 (pre-calcined and calcined)

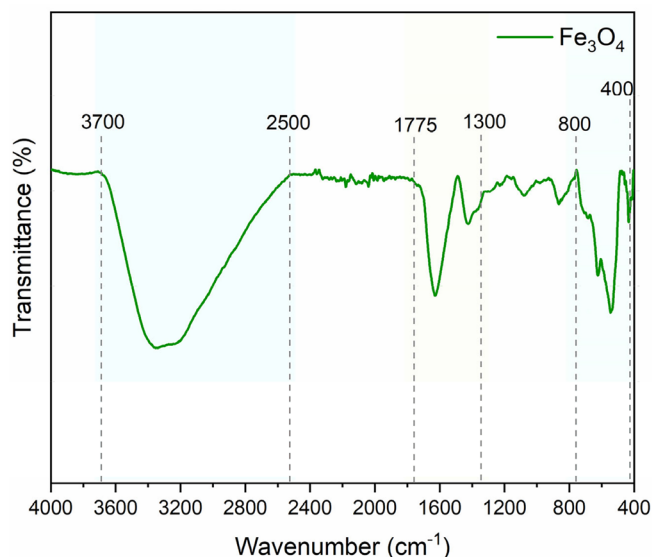


Figure 8. Infrared spectra of the magnetite sample (Fe_3O_4)

than the standard for hematite, while they had lower volume than the standard for magnetite. The results showed that pH played a significant role on the thermal behavior and structure of oxides, especially the crystallite size of hematite particles, with neutral or acidic pH being more attractive to obtain smaller particles. The obtained magnetite also presented a small crystallite size and magnetic characteristics without needing heat treatment, validating a simple synthesis with relatively low cost and high energy savings. Therefore, the results demonstrated that is possible to synthesize oxides with excellent structural properties using a more environmentally friendly method.

ACKNOWLEDGMENTS

To IFMA for the infrastructure and financial support (PRPGI notices No. 89/2021, No. 186/2021 and No. 287/2022). To the

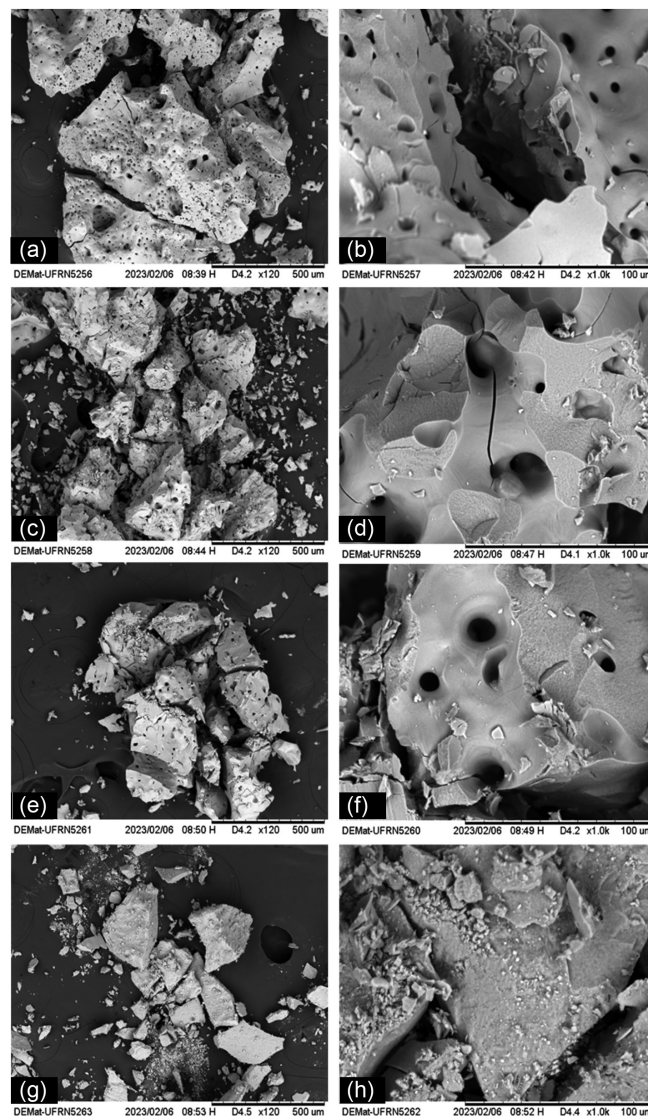


Figure 9. Micrographs of the $\alpha\text{-Fe}_2\text{O}_3$ samples obtained at pH 5 (a) 120 \times , (b) 1000 \times ; pH 7 (c) 120 \times , (d) 1000 \times ; pH 10 (e) 120 \times , (f) 1000 \times ; and the Fe_3O_4 sample (g) 120 \times , (h) 1000 \times

Department of Materials Engineering (DeMat-UFRN) and Tomaz R. de Araújo for the scanning electron microscopy analyses. CAPES for the scholarship granted in notice/CAPES No. 13/2020 (Support Program for the Development of Postgraduate Studies in the Legal Amazon). The co-authors thank FAPEMA, CNPq, and IFMA for the scientific initiation grants.

REFERENCES

1. Prestes, F. F.; *Brazilian Journal of Animal and Environmental Research* **2021**, *4*, 3848. [Crossref]
2. Paolino, C. C.; Amaral, F. G.; Cruz, C. B. M.; *Meio Ambiente (Brasil)* **2021**, *3*, 17. [Crossref]
3. Lachini, S. A.; Eslami, A.; *Int. J. Hydrogen Energy* **2024**, *51*, 51. [Crossref]
4. Mahmoud, M. E.; Amira, M. F.; Abouelanwar, M. E.; Salam, M. A.; *J. Environ. Chem. Eng.* **2021**, *9*, 104697. [Crossref]
5. Kunoh, T.; Takeda, M.; Matsumoto, S.; Suzuki, I.; Takano, M.; Kunoh, H.; *ACS Sustainable Chem. Eng.* **2018**, *6*, 364. [Crossref]
6. Nadagouda, M. N.; Hoag, G.; Collins, J.; Varma, R. S.; *Cryst. Growth Des.* **2009**, *9*, 4979. [Crossref]

7. Marco, B. A.; Rechelo, B. S.; Tófoli, E. G.; Kogawa, A. C.; Salgado, H. R. N.; *Saudi Pharm. J.* **2019**, *27*, 1. [Crossref]
8. Lenoir, D.; Schramm, K. W.; Lalah, J. O.; *Sustainable Chem. Pharm.* **2020**, *18*, 100313. [Crossref]
9. Juibari, N. M.; Eslami, A.; *J. Therm. Anal. Calorim.* **2017**, *130*, 1327. [Crossref]
10. Ahmad, S.; Munir, S.; Zeb, N.; Ullah, A.; Khan, B.; Ali, J.; Bilal, M.; Omer, M.; Alamzeb, M.; Salman, S. M.; Ali, S.; *Int. J. Nanomed.* **2019**, *14*, 5087. [Crossref]
11. Ying, S.; Guan, Z.; Ofoegbu, P. C.; Clubb, P.; Rico, C.; He, F.; Hong, J.; *Environ. Technol. Innovation* **2022**, *26*, 102336. [Crossref]
12. Rocha, M. B. C.; Araújo, T. R.; Medeiros, R. L. B. A.; Oliveira, M. M.; Figueredo, G. P.; *Research, Society and Development* **2021**, *10*, e399101623406. [Crossref]
13. Aarthye, P.; Sureshkumar, M.; *Mater. Today: Proc.* **2021**, *47*, 907. [Crossref]
14. Shamaila, S.; Sajjad, A. K. L.; Najam-ul-Athar, R.; Farooqi, S. A.; Jabeen, N.; Majeed, S.; Farooq, I.; *Applied Materials Today* **2016**, *5*, 150. [Crossref]
15. Pallela, P. N. V. K.; Ummey, S.; Ruddaraju, L. K.; Gadi, S.; Cherukuri, C. S. L.; Barla, S.; Pammi, S. V. N.; *Heliyon* **2019**, *5*, e02765. [Crossref]
16. Duarte, G. M.; Guilherme, L. R.; *Rev. Virtual Quim.* **2021**, *13*, 1069. [Crossref]
17. Rogez, H.; Akwie, S. N. L. T.; Moura, F. G.; Larondelle, Y.; *J. Food Sci.* **2012**, *77*, 1299. [Crossref]
18. Laurindo, L. F.; Barbalho, S. M.; Araújo, A. D.; Guiguer, E. L.; Mondal, A.; Bachtel, G.; Bishayee, A.; *Nutrients* **2023**, *15*, 989. [Crossref]
19. Sprenger, L. K.; Giese, E. G.; Santos, J. N.; Molento, M. B.; *Archives of Veterinary Science* **2016**, *21*, 21. [Crossref]
20. Cao, J.; Yin, C.; Qin, Y.; Cheng, Z.; Chen, D.; *J. Mass Spectrom.* **2014**, *49*, 1010. [Crossref]
21. Zhong, L.; Wu, G.; Fang, Z.; Wahlqvist, M. L.; Hodgson, J. M.; Clarke, M. W.; Junaldi, E.; Johnson, S. K.; *Food Res. Int.* **2019**, *116*, 1153. [Crossref]
22. Brunschwig, C.; Leba, L. J.; Saout, M.; Martial, K.; Bereau, D.; Robinson, J. C.; *Int. J. Mol. Sci.* **2017**, *18*, 61. [Crossref]
23. Nematalah, K. A.; Ayoub, N. A.; Abdelsattar, E.; Meselhy, M. R.; Elmazar, M. M.; El-Khatib, A. H.; Linscheid, M. W.; Hathout, R. M.; Godugu, K.; Adel, A.; Mousa, S. A.; *J. Funct. Foods* **2018**, *49*, 401. [Crossref]
24. Cao, C.; Yu, L.; Xie, Y.; Wei, W.; Jin, H.; *Int. J. Hydrogen Energy* **2022**, *47*, 8716. [Crossref]
25. Mirzaei, A.; Janghorban, K.; Hashemi, B.; Hosseini, S. R.; Bonyani, M.; Leonardi, S. G.; Bonavita, A.; Neri, G.; *Process. Appl. Ceram.* **2016**, *10*, 209. [Crossref]
26. Badnore, A. U.; Pandit, A. B.; *Chemical Engineering and Processing: Process Intensification* **2017**, *122*, 235. [Crossref]
27. Piro, N. S.; Hamad, S. M.; Mohammed, A. S.; Barzinjy, A. A.; *IEEE Trans. NanoBiosci.* **2023**, *22*, 308. [Crossref]
28. Selvaraj, R.; Pai, S.; Murugesan, G.; Pandey, S.; Bhole, R.; Gonsalves, D.; Varadavenkatesan, T.; Vinayagam, R.; *Appl. Nanosci.* **2021**, *11*, 2227. [Crossref]
29. Diniz, P. A. F.; Cavalcante, K. S. B.; Souza, J. C.; Marques, G. N.; Santos, F. H. S.; Cutrim, F. M.; Henriques, R. B.; Mendonça, L. T. B.; Nascimento, U. M.; *Mater. Res.* **2023**, *26*, e20230016. [Crossref]
30. Jacinto, M. J.; Silva, V. C. P.; Prescilio, I. C.; Correa, A. K.; Ferreira, L. F.; Razini, S. S.; *Anais Eletrônicos do 59º Congresso Brasileiro de Química*; João Pessoa, Brasil, 2019. [Link] accessed in March 2024
31. Buazar, F.; Baghlani-Nejzad, M. H.; Badri, M.; Kashisaz, M.; Khaledi-Nasab, A.; Kroushawi, F.; *Starch-Starke* **2016**, *68*, 796. [Crossref]
32. Darmawan, M. Y.; Istiqomah, N. I.; Adrianto, N.; Tumbelaka, R. M.; Nugraheni, A. D.; Suharyadi, E.; *Results Chem.* **2023**, *6*, 100999. [Crossref]
33. Mayedwa, N.; Mongwaketsi, N.; Khamlich, S.; Kaviyarasu, K.; Matinise, N.; Maaza, M.; *App. Surf. Sci.* **2018**, *446*, 266. [Crossref]
34. Karpagavinayagam, P.; Prasanna, A. E. P.; Vedhi, C.; *Mater. Today: Proc.* **2020**, *48*, 136. [Crossref]